Monthly Notices
of the
ROYAL ASTRONOMICAL SOCIETY

MNRAS **484,** 2198–2211 (2019)
Advance Access publication 2019 January 12

doi:10.1093/mnras/stz129

Experimental phase function and degree of linear polarization of cometary dust analogues

E. Frattin,[1,2]★ O. Muñoz,[3,4] F. Moreno,[3] J. Nava,[5] J. Escobar-Cerezo,[6] J. C. Gomez Martin,[3] D. Guirado,[3] A. Cellino,[7] P. Coll,[8] F. Raulin,[8] I. Bertini,[1] G. Cremonese,[2] M. Lazzarin,[1] G. Naletto[9,10,11] and F. La Forgia[1]

[1]*Department of Physics and Astronomy 'G. Galilei', University of Padova, Vicolo dell'Osservatorio 3, I-35122 Padova, Italy*
[2]*INAF, Astronomical Observatory of Padova, Vicolo dell'Osservatorio 5, I-35122 Padova, Italy*
[3]*Instituto de Astrofísica de Andalucía, CSIC, Glorieta de la Astronomia s/n, E-18008 Granada, Spain*
[4]*Advanced Optical Imaging Group, School of Physics, University College Dublin, Dublin 4, Ireland*
[5]*Department of Geosciences, University of Padova, Via G. Gradenigo 6, I-35131 Padova, Italy*
[6]*Department of Physics, University of Helsinki, FI-00014 Helsinki, Finland*
[7]*INAF – Astrophysical Observatory of Torino, Via Osservatorio 20, I-10025 Pino Torinese (TO), Italy*
[8]*Laboratoire Inter-Universitaire des Systemes Atmospheriques, Universites Paris 12 – Paris 7, CNRS, France*
[9]*Department of Physics and Astronomy 'G. Galilei', University of Padova, Via Marzolo 8, I-35131 Padova, Italy*
[10]*Center of Studies and Activities for Space (CISAS), 'G. Colombo', University of Padova, Via Venezia 15, I-35131 Padova, Italy*
[11]*CNR-IFN UOS Padova LUXOR, Via Trasea 7, I-35131 Padova, Italy*

Accepted 2018 December 22. Received 2018 December 20; in original form 2018 July 19

ABSTRACT

We present experimental phase function and degree of linear polarization curves for seven samples of cometary dust analogues namely: ground pieces of Allende, DaG521, FRO95002, and FRO99040 meteorites, Mg-rich olivine and pyroxene, and a sample of organic tholins. The experimental curves have been obtained at the IAA Cosmic Dust Laboratory at a wavelength of 520 nm covering a phase angle range from 3° to 175°. We also provide values of the backscattering enhancement for our cometary analogue samples. The final goal of this work is to compare our experimental curves with observational data of comets and asteroids to better constrain the nature of cometary and asteroidal dust grains. All measured phase functions present the typical behaviour for μm-sized cosmic dust grains. Direct comparison with data provided by the OSIRIS/Rosetta camera for comet 67P/Churyumov–Gerasimenko reveals significant differences and supports the idea of a coma dominated by big chunks, larger than one micrometer. The polarization curves are qualitatively similar to ground-based observations of comets and asteroids. The position of the inversion polarization angle seems to be dependent on the composition of the grains. We find opposite dependence of the maximum of the polarization curve for grains sizes in the Rayleigh-resonance and geometric optics domains, respectively.

Key words: scattering.

1 INTRODUCTION

Dust is a fundamental constituent of planetary systems in all their stages of development. For example, the origin of planetary systems involves a phase of aggregation of submicron-sized dust grains by streaming instability into protoplanetary discs (Johansen & Youdin 2007; Blum & Wurm 2008; Blum et al. 2014). In our mature Solar system, dust can be found in the interplanetary medium orbiting around the Sun as a product of the disintegration of comets and asteroidal collisional cascading (the Zodiacal Cloud), as well as in the rings of the giant planets. In addition, dust is present in the regolith surfaces of planets, asteroids and comets, and in dense atmospheres (e.g. Venus, the Earth, Mars, Titan) in the form of aerosol. Because of the ubiquity of dust and its involvement in countless physical phenomena, from atmospheric radiative transfer to cometary activity through the tracing of Solar system primitive materials, it is important to study its nature and properties.

Comets are the most appropriate targets to study the early Solar system, since they are among the most pristine objects orbiting

★ E-mail: elisa.frattin@gmail.com

the Sun. Because of their low velocity, gentle accretion process, some of their most primitive constituents (the grains) have remained intact, i.e. as they were when the comets formed (Fulle et al. 2016). During their passage at perihelion, these objects release refractory materials driven by the sublimation of trapped ices, generating a bright dust coma dominated by μm-sized particles composed of silicate minerals and organics. Comets unveil the composition of the primordial material from which they accreted, namely material located in the outer regions of the Solar system, and put some constraints to the processes involved in its origin. The flyby missions that first revealed the nature of cometary dust with *in situ* measurements were the *Giotto* (Reinhard 1986) and *Vega* (Sagdeev et al. 1986) missions to 1P/Halley in 1986. The 'Halley Armada' was followed up by the Deep Space 1 mission to comet 19P/Borrelly in 2001 (Soderblom et al. 2002). A major breakthrough came with the *Stardust* mission flyby of comet 81P/Wild in 2004 (Hörz et al. 2006), and subsequent return to Earth of samples of dust collected directly from the coma of the comet. Later, missions to comet 9P/Temple in 2005 (Deep Impact 2005; A'Hearn et al. 2005) and to comet 103P/Hartley in 2010 (EPOXI) (A'Hearn et al. 2011) provided new insights of these two objects. More recently, the Rosetta mission has been able, for the first time, to follow the trajectory of the cometary nucleus and observe its evolution during its trajectory before and after perihelion. The coma of comet 67P/Churyumov–Gerasimenko (hereafter 67P) was observed during two entire years (2014–2016) from the very inside, reaching distances of few km from the nucleus. The astonishing images obtained by the OSIRIS instrument onboard the spacecraft have shed new light into the properties of cometary dust (Sierks et al. 2015) . There is now evidence that 67P was formed by gentle accretion of pebbles smaller than 1 cm at velocities of the order of 1 $\mathrm{m\,s^{-1}}$ (Fulle & Blum 2017). Moreover, photometric analysis of the overall coma and single grains reveal that the majority of the material has similar spectral properties to those of nucleus surface (Frattin et al. 2017), which enables using the dust coma as a proxy indicator of nucleus properties.

The sunlight incident on a cometary dust envelope is partly absorbed and partly scattered by the particle cloud. Spacecraft and ground-based observations of scattered light show characteristics strictly dependent on the nature and physical properties (composition, size distribution, shape, roughness, etc.) of the material composing the coma. Since each material has characteristic scattering signatures, scattering theory can be used to interpret observations and retrieve from them some of the properties of the dust. Experimental data of the angular distribution of the scattered intensity and degree of linear polarization of clouds of cosmic dust analogues assist in the interpretation of *in situ* and remote sensing observations. Since these quantities are intimately related to the nature of the particles, laboratory data are used as a reference for comparison and interpretation, allowing a correct analysis of the observational data (Muñoz et al. 2000; Volten et al. 2006; Muñoz et al. 2017). Modelling of the interaction between electromagnetic radiation and particles in turn, supports the experiments, helping to discriminate unambiguously dust features corresponding to specific observables (Liu, Yang & Muinonen 2015; Zubko 2015; Escobar-Cerezo et al. 2017). All these different approaches (observations, laboratory experiments, and theoretical simulations) provide essential contributions to the investigation of the behaviour of dust particles as radiation scatterers.

In this work we present experimental phase function and degree of linear polarization curves as functions of the observational phase angle of a selected set of cometary dust analogues: four meteoritic samples, two minerals (Mg-rich olivine and pyroxene), and a sample of organic particles (tholins). Light scattering measurement has been performed at the Cosmic Dust Laboratory (CODULAB; Muñoz et al. 2011) at the Instituto de Astrofísica de Andalucía (IAA), spanning a phase angle range from 3° to 175° at a wavelength of 520 nm. We combine the new measurements presented in this work with the scattering matrices at 442 and 633 nm of a sample of the Allende meteorite and of size-segregated Mg-rich olivine samples that have been previously presented by Muñoz et al. (2000). Finally, we compare the experimental data with observations of asteroids and cometary dust envelops, with special emphasis on the observations of 67P by Rosetta, in order to put constraints on the nature of cometary dust.

2 LIGHT SCATTERING THEORY

A beam of quasi-monochromatic light is physically defined by the Stokes vector $\boldsymbol{I}= \{I, Q, U, V\}$, where I is proportional to the total flux of the light beam and Q is related to the linear polarization of the light beam, representing the difference between the two components of the flux along the x-axis and the y-axis. U is defined by the difference of the two components of the flux along the directions rotated by 45° from the x- and y-axis. V is related to the circular polarization, defined as the difference between the left-handed and the right-handed polarized components of the flux.

The interaction between a light beam and a cloud of particles results in scattering of the incident light. The Stokes vector of the scattered beam $\boldsymbol{I}_{sc}$ is related to the one of the incident beam $\boldsymbol{I}_{in}$ by the so-called scattering matrix $\mathbf{F}$, through the following expression:

$$\begin{pmatrix} I_{\rm sc} \\ Q_{\rm sc} \\ U_{\rm sc} \\ V_{\rm sc} \end{pmatrix} = \frac{\lambda^2}{4\pi^2 D^2} \begin{pmatrix} F_{11} & F_{12} & F_{13} & F_{14} \\ F_{21} & F_{22} & F_{23} & F_{24} \\ F_{31} & F_{32} & F_{33} & F_{34} \\ F_{41} & F_{42} & F_{43} & F_{44} \end{pmatrix} \begin{pmatrix} I_{\rm in} \\ Q_{\rm in} \\ U_{\rm in} \\ V_{\rm in} \end{pmatrix}, \quad (1)$$

where λ is the wavelength of the incident beam and D is the distance of the detector from the particles. The 16 dimensionless elements of the matrix depend on physical characteristics of the particles such as their number, shape, dimension (through the size parameter $x = 2\pi r/\lambda$) and refractive index, as well as on geometrical parameters such as their orientation in the space and scattering direction.

When the particles are randomly oriented all scattering planes are equivalent. Therefore, the scattering direction is fully described by the scattering angle, θ, defined by the angle between the directions of propagation of the incident and scattered beams. To facilitate direct comparison with astronomical observations of comets and asteroids we use the phase angle, $\alpha = 180^\circ - \theta$, throughout the text. Furthermore, when the particles present mirror symmetries, and are randomly oriented, the scattering matrix has six parameters (van de Hulst 1957):

$$\mathbf{F} = \begin{pmatrix} F_{11} & F_{12} & 0 & 0 \\ F_{12} & F_{22} & 0 & 0 \\ 0 & 0 & F_{33} & F_{34} \\ 0 & 0 & -F_{34} & F_{44} \end{pmatrix}. \quad (2)$$

3 EXPERIMENTAL APPARATUS

The CODULAB facility is dedicated to measuring the elements of the scattering matrix (equation 1 and 2) as a function of the scattering angle of clouds of randomly oriented cosmic dust analogues. This is

achieved by means of a gonio-nephelometer that has been described in detail previously by Muñoz et al. (2010). In the experiments carried out for this work we employed an Argon–Krypton laser tuned to 520 nm as our light source. The laser beam passes through a polarizer and an electro-optic modulator before encountering a jet stream of randomly oriented particles produced by an aerosol generator (Muñoz et al. 2011). The powder under analysis is contained in a cylindrical reservoir, and is pushed by a piston in a controlled manner towards a rotating brush, which disperses the particles into a flow of air which carries them through a nozzle to the scattering volume. The particle density in the scattering volume, which is controlled by the speed of the piston, must be high enough to produce a detectable scattering signal, but low enough to avoid multiple scattering. In this way it better approximates the low-density cometary coma. The scattered light passes through optional optics before being detected by a photomultiplier, the *detector*, which is mounted on a 1 m ring rail centred at the aerosol jet. In the measurements presented in this paper we have covered the phase angle range from 3° to 175° in steps of 5° within the 10°–20° and 40°–175° ranges, and in steps of 1° within the 3°–10° and 25°–40° ranges. Sinusoidal electro-optic modulation combined with lock-in detection allows determining all elements of the scattering matrix from eight different configurations of the optical components (equation 1) and the assumption of reciprocity of the sample (see further details in Muñoz et al. 2010). In order to keep the scattered intensity within the linearity range of the detector, a wheel of neutral density filters is placed between the laser head and the polarizer, which allows adapting the beam intensity to the scattering behaviour of the aerosol sample at each particular angle. A second photomultiplier placed at a fixed angle, the *monitor*, corrects for fluctuations in the aerosol beam. For each position of the detector, 1000 measurements are conducted in about 2 s. The final value at each phase angle is obtained from the average of such measurements, with an associated error given by the standard deviation. Three measurement runs are carried out for each optical configuration in order to achieve further noise reduction. Due to the limited amount of material, we did not measure the complete scattering matrix but only the elements F_{11} and F_{12}. For unpolarized incident light the F_{11} is proportional to the scattered flux. The measured values of the F_{11} are arbitrarily normalized so that they are equal to 1 at $\alpha = 150°$. The F_{11} normalized in this way is called the *phase function*. The $-F_{12}/F_{11}$ ratio (where the value of F_{11} is not normalized) is equal to the degree of linear polarization, P, for unpolarized incident light, expressed in terms of Stokes parameters as $P = -Q_{sc}/I_{sc}$.

4 MATERIALS

We have selected four Carbonaceous Chondrites (CCs), two silicate minerals, and one organic powder as sources of cometary dust analogues. Bulk samples of the meteorites DaG521, FRO95002, and FRO99040 were provided by the Museo dell'Antartide Felice Ippolito, Siena especially for this work. Batches of particulate tholins were synthesized at the Laboratoire Inter-Universitaire des Systemes Atmospheriques (LISA), Paris. The Allende, olivine, and pyroxene samples belong to the IAA-CODULAB collection and have been used in a previous work (Muñoz et al. 2000). Below we describe the bulk properties of these materials, the methods employed to obtain particulate samples suitable for our light scattering experiments, and the physical properties of the particles (optical constants, size distribution, and morphology).

Table 1. Mean composition of CV and CO chondrites and of the Allende meteorite in per cent wt, taken from the meteorite data base METDB (Nittler et al. 2004).

	CO	CV	Allende
Si	15.8	16.0	16.0
Ti	0.08	0.15	0.10
Al	1.58	2.19	1.79
Cr	0.36	0.35	0.37
Fe	24.3	23.1	23.9
Mn	0.18	0.15	0.15
Mg	14.4	14.4	15.0
Ca	1.62	2.5	1.89
K	0.05	0.03	0.03
S	1.94	1.63	1.77
P	0.11	0.13	0.10
Na	0.35	0.35	0.33
Ni	1.31	1.11	1.23
O	37.9	37.9	37.2

4.1 Bulk materials description

4.1.1 Meteorites

CCs meteorites are among the oldest and most primitive materials in the Solar system. Age determination techniques indicate that they formed around 4.5 Gyr ago (Chen & Wasserburg 1981; Mahnes, Göpel & Allégre 1987). Since they are very old, these rocks suffered different primary processes, which record pre-accretionary histories in the solar nebula, and secondary processes like aqueous alteration, thermal metamorphism, and shock metamorphism (Brearley & Jones 1998).

CCs are divided in several classes based on composition: CI, CH, CO, CV, CK, CR. Most of them are fragments of primitive asteroids. They come from the NEO population, which includes about 10 per cent of extinct comets, in addition to former asteroids (DeMeo & Binzel 2008).

The bulk composition of the Carbonaceous Ivuna (CI) group of chondrites is very close to the composition of the solar photosphere. Furthermore, interstellar grains that predate the Solar system formation are found in the matrix of these primitive chondrites (Brearley & Jones 1998). CCs are characterized by chondrule sizes ranging from 1 mm in the CV group down to around 0.15 mm and 0.02 mm in the CO and CH groups, respectively. The CV and CO chondrites have the highest abundances of refractory inclusions, while CR and, above all, CH chondrites have the highest content of metals (Brearley & Jones 1998; Weisberg, McCoy & Krot 2006). In Table 1 we report the mean composition of CO and CV chondrites and of the Allende meteorite (Nittler et al. 2004).

*DaG521 and Allende*The meteorites DaG521 (Dar al Gani 521, found in Lybia in 1997; Grossman 1999) and Allende (fallen near Parral, Chihuahua, Mexico, in 1969) are classified as CV3. CVs chondrites are characterized by large mm-sized chondrules, large refractory inclusions, and abundant matrix (40 per centvol). They are divided into oxidized CV_{OX} and reduced CV_{RED} subgroups based on abundances of metal, magnetite, and Ni content (McSween 1977). The main component of CV matrices is Fe-rich olivine (fayalite Fa ∼ 30–60 and in some cases Fa > 90), but there are substantial differences among the subgroups due to different late stage metasomatism and aqueous alteration (Krot, Scott & Zolensky 1995; Krot et al. 1998). Other mineral constituents are Ca-Fe-pyroxene, andradite, Fe-Ni sulfides, and magnetite. Some chemical

and textural features of the CV chondrites evidence a phase in which the parent body experienced temperatures <300°C (Krot et al. 1998).

DaG521 is the only meteorite of our set with reddish colour, probably due to iron oxide generated by weathering in the Lybian desert.

Allende is classified as CV_{OX}. This group displays Calcium-Aluminum-rich Inclusions (CAIs) and ameboid olivine refractory elements and this suggests they have been formed at high temperature during the early stages of Solar system formation. A recent discovery of a class of asteroids (the so-called Barbarians) seems to have a composition unusually enriched in CAI minerals, like spinel (Cellino et al. 2014). Allende differs from other CV_{OX} meteorites in its lower matrix-chondrule ratio and in having chondrules with more opaque minerals (Brearley & Jones 1998).

*FRO95002 and FRO99040*These two meteorites were found in Antarctica, in the region of the Frontier Mountain in 1995 and 1999, respectively. Both belong to the CO3 class, which presents similar characteristic of CV3 regarding chondrules and matrix abundance, but differ in the chondrule dimensions, which in the CO3 case are μm sized. The CO chondrites are all of petrologic type 3, showing slightly different metamorphic stages, ranging from 3.0 to 3.7 (McSween 1977). CO chondrites usually have low Fe compositions with olivine with Fa < 1 (Brearley & Jones 1998). Also Fe-pyroxenes are rare, only a few pyroxenes with Fs ∼ 10 are reported (Brearley & Jones 1998).

4.1.2 Minerals

The first hint of the presence of silicates in the cometary dust dates back to the observation of the emission feature at 10 μm in comet Bennett and its consequent laboratory modelling (Maas, Ney & Woolf 1970). The measurements of 1P/Halley mineralogical composition revealed Mg-rich olivine (forsterite) and pyroxene (enstatite) as dominant compounds from *in situ* mass spectra of particles provided by *Giotto* and *Vega* Spacecraft (Schulze, Kissel & Jessberger 1997). Crystalline forsterite and enstatite have been detected also on comet Hale–Bopp (Crovisier et al. 1997) and 9P/Tempel from space-based infrared spectra (Lisse et al. 2007) and on 81P/Wild2 from direct measurement of particles collected by Stardust mission (Zolensky et al. 2006). These silicates are predicted by thermodynamic models to condense in a hot gas at 1200–1400 K, while the reaction with Fe occurs only at lower temperature. Thus, the preponderance of Mg-rich silicates in cometary dust can be explained by direct condensation in the inner primordial nebula (Hanner & Bradley 2004). The olivine and pyroxene samples used in this work have, respectively, the composition $Mg_{1.85}Fe_{0.14}SiO_4$ and $Mg_{0.85}Fe_{0.08}Si_{0.99}O_3$, and are therefore close to the Mg-rich endmembers, i.e. forsterite and enstatite. Thus, in the following we will refer to the olivine and pyroxene samples as forsterite and enstatite. The forsterite sample is the one identified as 'Olivine S' in Muñoz et al. (2000).

4.1.3 Organics

Tholins are organic compounds generated by irradiation (solar UV, high energy particles, electrons) of mixtures of common compounds of carbon, oxygen, and nitrogen, e.g. CO_2, CH_4, and HCN (Sagan & Khare 1979). They are thought to be present on the surfaces and/or in the atmospheres of several Solar system bodies. For example, they are likely responsible for the reddish colour of many objects such as Pluto (Gladstone 2016) and Ceres (Combe et al. 2017), and are believed to be responsible for Titan's atmospheric haze (Brassé et al. 2015).

Analysis of 1P/Halley dust mass spectra indicated for the first time the existence of CHON particles in comets (Kissel & Krueger 1987). The complex nature and variety of organics in cometary dust was revealed by analysis of samples returned from 81P/Wild, obtained by *Stardust* (Sandford et al. 2006; Matrajt et al. 2008; Clemett et al. 2010). More recently, the *in situ* analysis of 67P coma dust by COSIMA/*Rosetta* mass spectrometer has confirmed the presence of abundant high-molecular weight organic matter, nearly 50 per cent in mass (Bardyn et al. 2017; Fray et al. 2017). Thus, the abundance of CHON compounds in cometary dust suggests that tholins are likely to form in this environment as well. Tholins have been previously used in laboratory studies as cometary dust simulants, often mixed with other components, typically silicates and ices (Poch et al. 2016a,b; Jost et al. 2017).

The tholins sample used in this work was synthesized using the PLASMA experimental set-up described previously by Brassé et al. (2017). It allows the production and sampling of tholins from N_2–CH_4 electron irradiation in a glove box without contamination by the air of the laboratory. The elemental composition of these tholins has been determined (Brassé 2014). They are carbon rich (C/N = 2.2 to 2.4) with a C/H of 0.7 to 0.8. Several grams of tholins were prepared to perform the CODULAB measurements.

4.2 Sample preparation

In order to obtain particulate samples with different size distributions within the typical size range of cosmic dust particles, the DaG521, FRO95002, and FRO99040 samples were milled and dry sieved at the Department of Geoscience of the University of Padua. After milling, the three samples were first size segregated using a 71 μm sieve. The fraction of sample that passed through the sieve was subsequently sieved using a 53 μm sieve. This procedure generated three subsamples designated as DaG521M, FRO99040M, and FRO95002M with diameters, d, in the range 53 μm < d < 71 μm. The fractions of DaG521M and FRO99040M that passed through the 53 μm sieve were subsequently sieved through a 45 μm sieve producing subsamples DaG521S and FRO99040S (45 μm < d < 53 μm). Not enough material of FRO99040M was left to produce a further sample. A similar sieving procedure was used to produce the olivine samples described by Muñoz et al. (2000).

As far as the organic sample is concerned, after their synthesis, the tholins were kept in gas proof vials under dry N_2 atmosphere, to avoid their chemical evolution. Just before measurements with CODULAB the tholins were first homogenized with a mortar to break the agglomerates and sieved to obtain an homogeneous powder. Then, these tholins were introduced into the cylindrical stainless steel tank of the aerosol generator.

4.3 Sample characterization

4.3.1 Refractive index

The refractive index of a medium is defined as

$$m = c\sqrt{\epsilon\mu} = n + ik \tag{3}$$

where ε is the electric permittivity, μ is the magnetic permeability, and c the speed of light in vacuum. The optical constants n and k

Table 2. Refractive index of each sample and their relative appearance.

Sample	Refractive Index	Appearance
DaG521	$1.65 + i10^{-3}$	reddish
FRO99040	$1.65 + i10^{-3}$	dark grey
FRO95002	$1.65 + i10^{-3}$	dark grey
Allende	$1.65 + i10^{-3}$	dark grey
Forsterite	$1.62 + i10^{-5}$	white
Enstatite	$1.58 + i10^{-5}$	white
Tholins	$1.35 + i2.3 \cdot 10^{-2}$	dark

represent, respectively, the phase velocity of the wave in the medium and the absorption coefficient of the material.

Estimates of the refractive indices of our samples are compiled in Table 2. The refractive indices of forsterite and enstatite (Dorschner et al. 1995) have been obtained from the Jena-St. Petersburg Data base of Optical Constants (http://www.astro.uni-jena.de/Laboratory/Database/jpdoc/index.html). The refractive index of tholins at 532 nm has been reported by Hasenkopf et al. (2010); for a detailed analysis of the tholins optical properties see Brassé et al. (2015).

The refractive indexes of the Allende, DaG521, FRO99040, and FRO95002 meteorite samples are unknown. Therefore, we have assumed estimates based on literature values of the main constituents. The imaginary part of the refractive index of the terrestrial samples is significantly smaller than that of the meteorites and tholins, which indicates a smaller absorbance of these materials, consistent with their light colour. By contrast, the meteorite powders are darker as a result of the higher bulk Fe content and organic components.

It should be kept in mind that the refractive index generally depends on the wavelength of the incident light. While the Mg-rich forsterite and enstatite present a flat wavelength dependence in the visible, the Fe content of the meteorite samples is expected to produce an effect on the refractive index at different visible wavelengths. This fact has been recently taken into account by Devogèle et al. (2018) to interpret the observed wavelength dependence of the inversion angle of polarization of asteroid (234) Barbara as a consequence of the imaginary refractive index, in turn a consequence of the presence of nano-iron phase particles.

4.3.2 Size distribution

The size distributions of our samples have been estimated using a low angle laser light scattering (LALLS) particle sizer (Malvern Mastersizer 2000; Rawle 1993). The LALLS method relies on the measurement of the phase function of samples dispersed in a carrier fluid at 633 nm within a range of low scattering angles (0.02°–30°). The volume distribution of equivalent spherical particles that best reproduces the observed phase function is obtained by inverting a light scattering model based on Mie theory, which requires knowing the complex refractive index of the samples (equation 3). Since the refractive indexes of our meteorite samples are unknown, we have carried out a sensitivity study of the impact on the retrieved size distributions of varying n and k within wide ranges. In these sensitivity tests we have used as reference value the estimated refractive index for the Allende meteorite ($m = 1.65$, $k = i0.001$; Muñoz et al. 2000). First, the imaginary part of the refractive index, k, was fixed to the reference value ($k = 0.001$). The value of real part, n, was then varied between 1.5 and 1.7

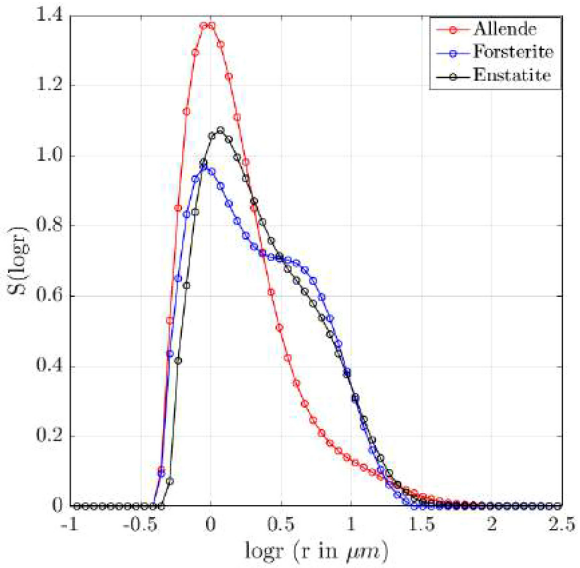

Figure 1. Size distribution of samples of Allende meteorite, Forsterite, and Enstatite.

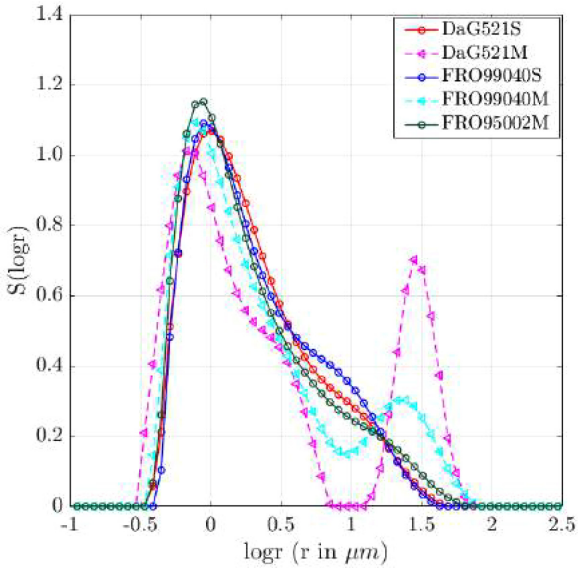

Figure 2. Size distribution of two different samples of DaG521, FRO95002, and FRO99040.

in steps of 0.05. Second, the real part was fixed to the reference value ($n = 1.65$), and the imaginary part, k, was varied from 10^{-5} to 10^{-1} in factor of 10 steps. Artefacts are found in the retrieved size distributions in the small size range ($r < 1$ μm) when low values of the real part ($n = 1.5$; $n = 1.55$) or extreme values of the imaginary part ($k = 10^{-5}$; $k = 10^{-2}$; $k = 10^{-1}$) are assumed. Therefore, we consider the reference value $n = 1.65 + i0.001$ as a reasonable estimate of the refractive index of our meteorite samples.

In spite of the sieving procedure described in Section 4.2, the meteorite samples show broad size distributions with volume equivalent radii ranging from 0.3 to ∼ 100 μm. Figs 1 and 2 show the $S(\log r)$ size distributions of the samples. Here, $S(\log r)$ is the projected surface area for a volume equivalent sphere with radius

r. Size distributions are commonly characterized by the effective radius $r_{\rm eff}$ and effective variance $v_{\rm eff}$ as defined by Hansen & Travis (1974). These parameters have a straightforward interpretation for mono-modal distributions, while for multimodal distributions, the $r_{\rm eff}$ and $v_{\rm eff}$ are only first-order indicators of the particles size. For example, the DaG521M and FRO99040M samples show bi-modal size distributions with secondary peaks at ∼30 and ∼20 μm, respectively.

Due to the limited amount of the tholins sample, we could not measure its size distribution. Based on the Field Emission Scanning Electron Microscope (FESEM) images (Figs 3k and 3l) we can estimate a broad size distribution with sizes ranging from submicron up to hundred of microns.

4.3.3 Morphology

Fig. 3 shows Field Emission Scanning Electron Microscope (FESEM) images of our samples. It can be seen that in all cases the particles present a wide variety of irregular shapes. Figs 3(a)–(d) show that the enstatite, forsterite, and Allende meteorite particles present sharp edges and relatively clean flat surfaces compared with the other samples. The DaG521, FRO95002, and FRO99040 particles (Figs 3e–j) present more rounded shapes with rough surfaces covered by a layer of small particles. These morphological differences could be partially caused by the powder preparation method. The dry-sieving procedure could not remove small particles that remained stuck on the surface of the large particles by electrostatic forces. By contrast, the enstatite, forsterite, and Allende meteorite samples underwent wet sieving, which removed a large fraction of the finest particles from the original sample. For this reason the grain surfaces appear generally smoother than for the other samples. Tholins show peculiar structures due to the synthesis process that produced very elongated particles of the order of 10 μm with layered substructure and sub-μm surface roughness (Figs 3k–l).

5 RESULTS AND DISCUSSION

5.1 Measurements

In this section we present the measured phase functions $F_{11}(\alpha)$ (Fig. 4) and degree of linear polarization for unpolarized incident light $P(\alpha) = -F_{12}(\alpha)/F_{11}(\alpha)$ (Fig. 5) for all samples studied in this work. The measurements were performed at a wavelength of 520 nm covering the phase angle range from 3° to 175°. As mentioned, the measured phase functions are normalized to unity at $\alpha = 150°$. The experimental phase function and polarization curves are freely available in the Amsterdam–Granada Light Scattering Data base (http://www.iaa.es/scattering) under request of citation of this paper and Muñoz et al. (2012).

The light scattering behaviour of the samples considered in this work is qualitatively similar to that of other types of irregular mineral dust investigated in the laboratory (see Muñoz et al. 2012 and references therein). The measured phase functions show a strong peak at large phase angles, a plateau with almost no structure at intermediate angles, and a moderate increase at small phase angles. Fig. 4 does not reveal large differences between samples.

The measured P curves display the typical bell shape with a small negative branch starting at an inversion angle, α_0 and reaching a minimum at $\alpha_{\rm min}$ (Fig. 5). The wide positive branch has a maximum $P_{\rm max}$ at $\alpha_{\rm max} = 75°$–$90°$. These polarization curves are also similar to those observed by remote sensing for a variety of Solar system objects such as comets and asteroids. In contrast to the phase functions, the polarization curves of our samples do show significant variability. Table 3 summarizes the main parameters of the degree of linear polarization curve in the region of minimum polarization ($P_{\rm min}$, $\alpha_{\rm min}$), inversion angle (α_0), and maximum polarization ($P_{\rm max}$, $\alpha_{\rm max}$).

Among our samples, tholins show the highest maximum values of linear polarization ($P_{\rm max} = 19$ per cent) and the deepest negative branch ($P_{\rm min} = -6.7$ per cent). Note that the empirical relationship known as *Umov's effect* indicates an inverse relationship between the maximum value of polarization and the geometric albedo (Zubko et al. 2011), and tholins are indeed the darkest material considered in this study. However, for a cloud of irregular particles in single scattering conditions the interrelation between $P_{\rm max}$ and the geometric albedo is dependent on the size distribution of the particle cloud (Zubko et al. 2017, 2018). Thus, the Allende meteorite sample, which has the smallest effective radii, also presents the lowest maximum of the degree of linear polarization in spite of its dark colour. Interestingly, the polarization curve of the Allende sample has a distinct feature compared to the pure silicate samples, showing a shoulder near $\alpha = 150°$ at all wavelengths (see Fig. 6). The measured values of α_0 range from 26° for enstatite to 36° for the Allende sample. We do not find a clear relation between size distribution and position of the inversion angle. By contrast, for the range of sizes of our samples, the location of the inversion angle seems to be dependent on the composition. Terrestrial materials consisting of pure non-absorbing minerals show lower inversion angles than the meteorites and tholins, which present iron and organic material in different proportions.

A fully satisfactory explanation of the negative branch of the linear polarization curve is still missing. Numerous Solar system objects such as cometary comae or asteroids and satellites, which are covered by a thick regolith layer, show this feature. Even quite small asteroids, for which we might assume that the surface regolith layer is thinner, generally exhibit the same general polarimetric behaviour as larger asteroids.

In principle, each powdered material should produce negative values of polarization at low phase angles, when coherent backscattering by small particles is considered. This physical effect results from the interference of wavelets scattered by the particulate medium. At zero phase angle the wavelets are in phase and they combined positively enhancing the intensity. The linear polarization reflects this effect as well, inverting the plane of wave polarization and favouring the parallel component of electromagnetic wave to be scattered, rather than the perpendicular one. The role of coherent backscattering in the development of a negative polarization branch and a backscattering enhancement (BSE) in the phase function has been discussed by Muinonen et al. (2012) using the exact method known as the superposition T-Matrix (Mackowski & Mishchenko 1996).

The origin of the negative branch of clouds of particles in single scattering conditions and corresponding particulate surfaces has also been investigated in several laboratory studies (e.g. Shkuratov et al. 2006, 2007; Escobar-Cerezo et al. 2018). In a recent work, Escobar-Cerezo et al. (2018) compare the scattering behaviour of two samples of the same lunar simulant with different size distributions. The effect of removing particles smaller than ∼1 μm from the pristine sample on the polarization curve is noticeable. The maximum of the linear polarization increases by a factor of 1.5. Apparently the small particle fraction of the pristine sample was

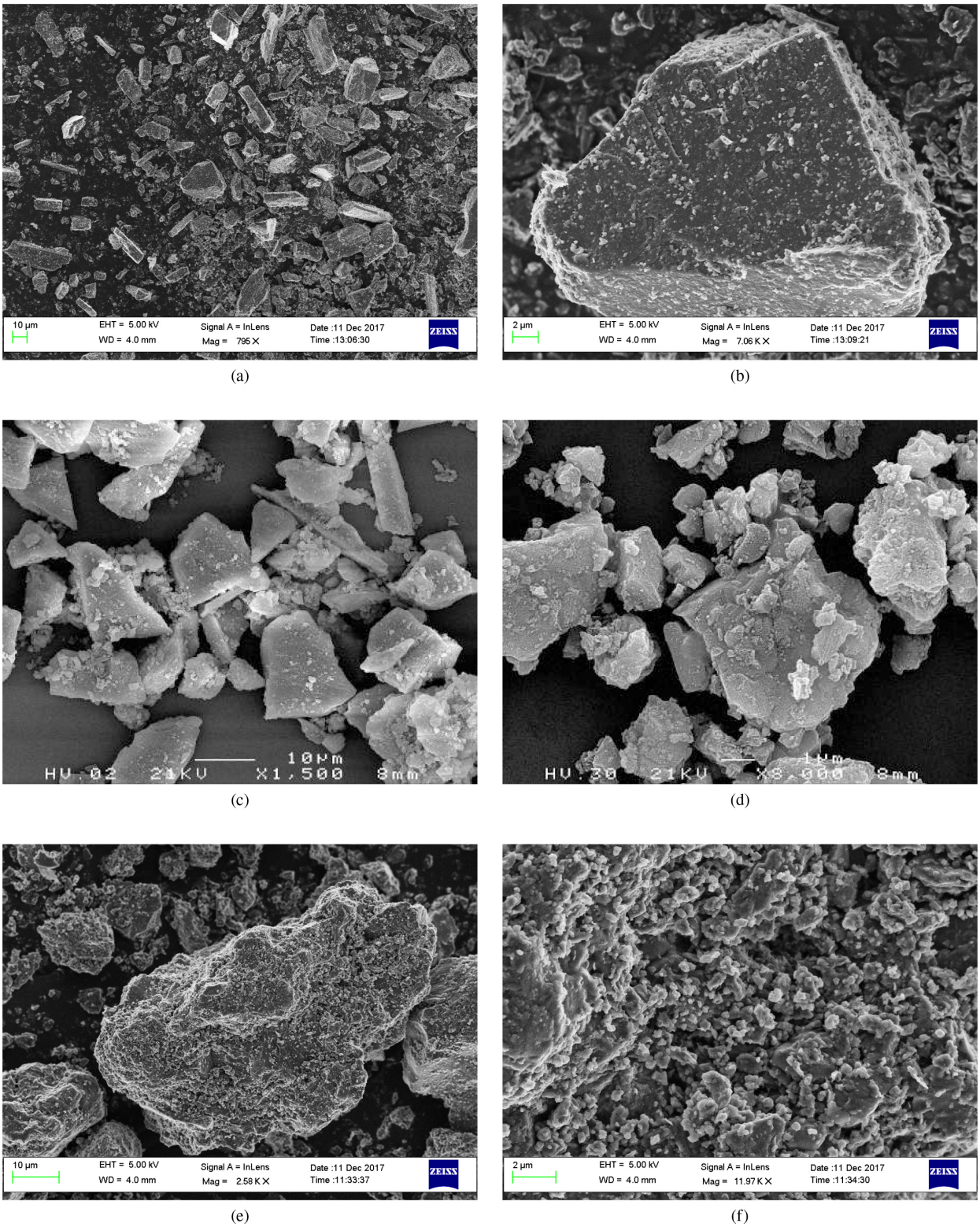

Figure 3. FESEM micro-photographs of enstatite (plates **a** and **b**), forsterite (plate **c**), Allende (plate **d**), DaG521 (plates **e** and **f**), FRO95002 (plates **g** and **h**), FRO99040 (plates **i** and **j**), and tholins (plates **k** and **l**).

limiting the maximum of the degree of linear polarization. Further, the negative polarization branch (absolute values) is decreased from 2.4 per cent to 0.8 per cent after removing particles smaller than 1 µm. This result seems to indicate that submicron scale features might be responsible for the negative branch of the degree of linear polarization.

In summary, it is quite difficult to disentangle all the effects responsible for the polarization curve shape, we can only highlight

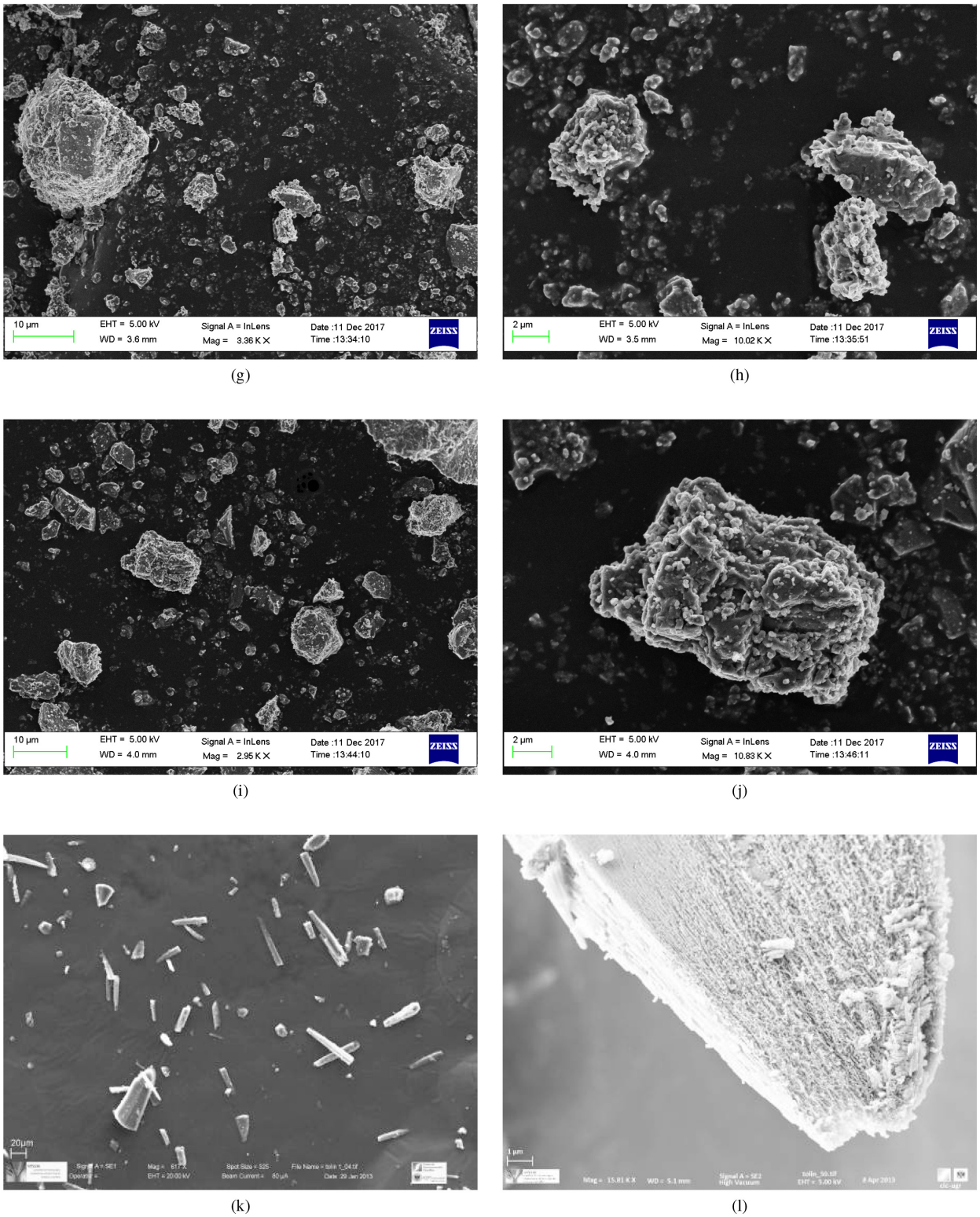

Figure 3 – *Continued*

some empiric relations, but it is essential to further investigate the subject. In sections 5.2 and 5.3 the differences observed in the phase function and degree of linear polarization are discussed in terms of different physical properties (size, colour, shape), in order to investigate their influence on the scattering behaviour of the samples.

5.2 Backscattering enhancement

In order to give an estimation of the trend of the phase function in the backward region for all studied samples, we compute the BSE, defined as the ratio of measured phase function values at $\alpha = 0^\circ$ and $\alpha = 30^\circ$ (Bertini, Thomas & Barbieri 2007). Since

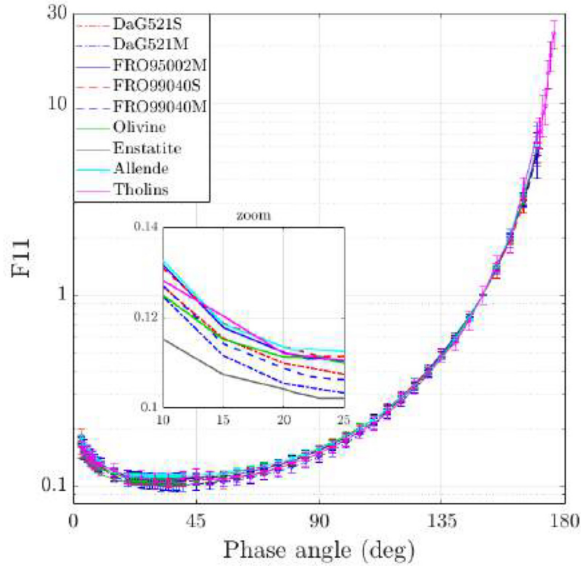

Figure 4. Phase functions of all samples at 520 nm. The inset shows a zoom-in of the backscattering region.

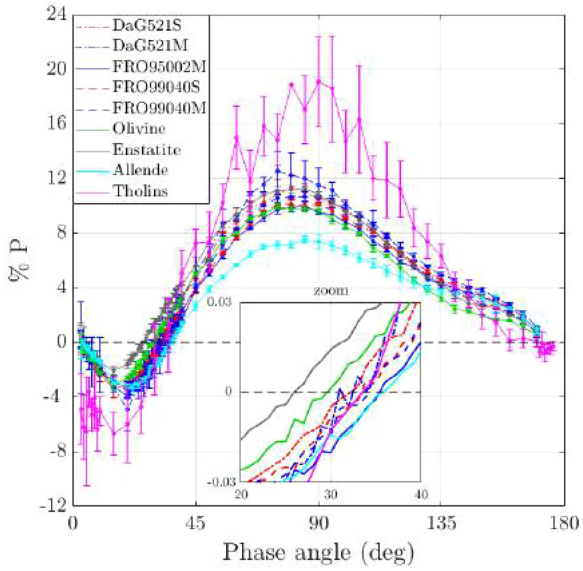

Figure 5. Polarization curve of all samples at 520 nm. The inset shows a zoom-in of the inversion angle region.

our laboratory measurements do not cover the whole phase angle range we extrapolated a synthetic phase function, $F_{11}^{\rm syn}$, from our measurements that range from 3° to 175°. The synthetic phase function is defined in the full angle range from 0° to 180° and is normalized according to

$$\frac{1}{2}\int_0^{\pi} {\rm d}\alpha \sin\alpha F_{11}^{\rm syn}(\alpha) = 1. \quad (4)$$

The extrapolation of the measured phase function in the forward direction is based on the assumption that the forward scattering peak for randomly oriented particles with moderate aspect ratios is mainly dependent on the size and refractive indices of the particles, but not on their shapes (Liu et al. 2003). Between 175° and 180°, we produce Mie calculations for projected surface area equivalent spheres. For the Mie computations we use the measured size distribution of the corresponding sample and the value of the refractive indices presented in Table 2. For the backward direction, we first generate a value for the phase function at 0° by a quadratic function generated by least squares with the measured data points from 3° to 30°. Then all values between 3° and 30° are produced by a cubic splines interpolation considering an additional condition that must be fulfilled in all cases: the first derivative of the phase function at 0° must be zero (Hovenier & Guirado 2014). At this stage, both the forward peak (175°–180°) and the rest of the phase function (0°–175°) are defined, but they are normalized in a different way: the forward peak belongs to a function normalized according to equation (4) and the normalization of the rest of the function is arbitrary. The function defined by the measured (3°–175°) plus the extrapolated (0°–3°) data points is then vertically shifted until the computed $F_{11}^{\rm syn}(175°)$ matches the measured $F_{11}(175°)$. The normalization condition (equation 4) is then checked. If it is not satisfied within a 0.1 per cent accuracy, the value of the measurement at 175° is increased or decreased (within the experimental error bars) until the normalization condition is fulfilled. The BSE for all our samples lays in the range [1.94–2.27] (see Table 4).

5.3 The effect of size and colour on polarization

The degree of linear polarization of the DaG521S and DaG521M, and the FRO99040S and FRO99040M samples are plotted in Figs 7 and 8, respectively. Since each figure refers to the same material, the differences observed are only attributable to the different size distributions of the S and M samples. The salient feature of this comparison is an increase of the maximum polarization with size. In fact, it can be seen in Fig. 2 that the size distributions of the samples with a higher $P_{\rm max}$ (DaG521M and FRO99040M) present a secondary maximum at larger sizes. Thus, the contribution of particles with large size parameters ($x_{\rm eff} = 2\pi r_{\rm eff}/\lambda$) is most likely responsible for the measured increase in $P_{\rm max}$.

The direct relationship between $P_{\rm max}$ and $r_{\rm eff}$ (or $x_{\rm eff}$) apparent in Figs 7 and 8 suggests an inverse relationship between $P_{\rm max}$ and wavelength, since the size parameter is inversely proportional to wavelength.

The polarization curves for the forsterite sample at three different wavelengths (442, 520, and 633 nm) are plotted in Fig. 9. The measurements at 442 and 633 nm have been published previously (Muñoz et al. 2000). It can be seen that $P_{\rm max}$ increases as the size parameter of the particles decreases (λ increases for a fixed $r_{\rm eff}$). In this case the differences in the measured degree of linear polarization are also likely related to the size parameter of the grains, since the refractive index of forsterite presents a flat dependence on wavelength in the studied region.

The apparent contradiction between Figs 7 and 8 on one side and Fig. 9 on the other can be explained by the broad size range of our samples. The scattering properties of dust grains are described by three regimes: Rayleigh, resonance, and geometric optics. When particles are smaller than the wavelength (Rayleigh regime), $P_{\rm max}$ tends to decrease as the size parameter increases. In that case, $P_{\rm max}$ increases with wavelength if the refractive index is constant, i.e. $P_{\rm max} \propto 1/x \propto \lambda$. By contrast, in the geometric optics regime ($x_{\rm eff} \gg \lambda$), $P_{\rm max}$ tends to increase as the size parameter becomes larger, i.e. $P_{\rm max} \propto x \propto 1/\lambda$. These trends are well illustrated by computed polarization data for Gaussian random shapes from the Rayleigh to the geometric optics regimes reported by Liu et al. (2015). As shown in Fig. 2, the contribution of grains in the geometric optics domain for samples DaG521M and FRO95002M is relatively large.

Table 3. Polarimetric parameters of the samples. $r_{\rm eff}$ and $v_{\rm eff}$ are the effective radius and effective variance. $P_{\rm min}$ is the minimum of polarization and $\alpha_{\rm min}$ the relative phase angle. $P_{\rm max}$ is the maximum of polarization at phase angle $\alpha_{\rm max}$ and α_0 is the inversion angle. h(per cent/deg) is the slope of the polarization curves computed between $\alpha_{\rm max}$ and α_0. Tholins measurements were taken in the red domain, at $\lambda = 632$ nm.

Sample	$r_{\rm eff}$ (μm)	$v_{\rm eff}$	$P_{\rm min}$ (per cent)	$\alpha_{\rm min}$ (deg)	α_0 (deg)	$P_{\rm max}$ (per cent)	$\alpha_{\rm max}$ (deg)	h (per cent/deg)
DaG521S	3.58	1.96	-3.3 ± 0.7	15 ± 5	32 ± 1	11.3 ± 0.91	80 ± 5	0.24
DaG521M	8.69	2.43	-4.9 ± 1.6	20 ± 5	34 ± 1	12.6 ± 1.4	75 ± 5	0.31
FRO95002M	3.92	2.72	-3.9 ± 0.1	20 ± 5	35 ± 1	10.0 ± 0.3	85 ± 5	0.20
FRO99040S	3.68	1.72	-3.3 ± 0.3	20 ± 5	33 ± 1	10.1 ± 0.3	80 ± 5	0.21
FRO99040M	5.90	3.10	-3.5 ± 0.6	20 ± 5	34 ± 1	10.7 ± 0.1	90 ± 5	0.19
Forsterite	3.06	1.04	-3.1 ± 0.3	15 ± 5	30 ± 1	9.9 ± 0.2	75 ± 5	0.22
Enstatite	3.70	3.13	-2.1 ± 0.3	15 ± 5	26 ± 1	11.3 ± 0.2	85 ± 5	0.19
Allende	2.44	3.42	-3.3 ± 0.3	22 ± 1	36 ± 1	7.5 ± 0.2	85 ± 5	0.15
Tholins	-	-	-6.7 ± 1.5	15 ± 5	35 ± 1	19.1 ± 3.3	90 ± 5	0.35

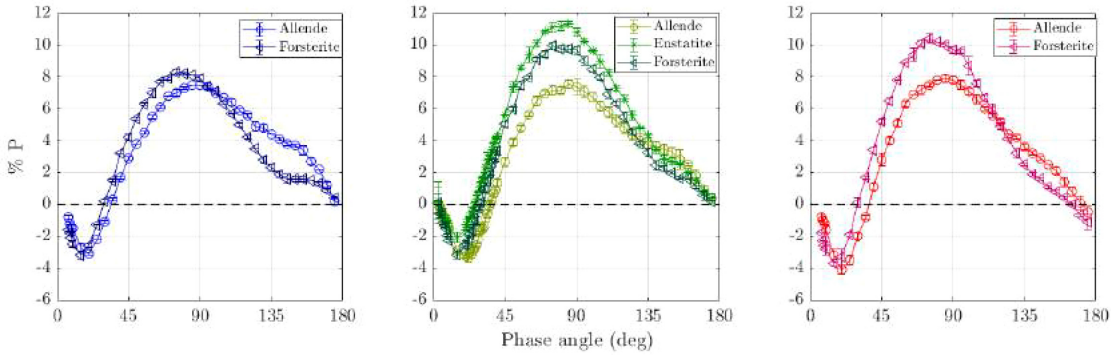

Figure 6. Measured degree of linear polarization curves for Allende meteorite (circles), forsterite (triangles), and enstatite (stars) at three different wavelengths 442 (left-hand panel), 520 (centre panel), and 633 (right-hand panel).

Table 4. Parameters related to the BSE computed for the samples at different wavelengths. BSE $= F_{11}(0^\circ)/F_{11}(30^\circ)$.

Sample	$r_{\rm eff}$ (μm)	$v_{\rm eff}$	$x_{\rm eff}$	$F_{11}^{\rm syn}(0^\circ)$	$F_{11}^{\rm syn}(30^\circ)$	BSE (520 nm)
DaG521S	3.58	1.96	43.3	0.384	0.191	2.01
DaG521M	8.69	2.43	105.0	0.419	0.214	1.96
FRO95002M	3.92	2.72	47.4	0.390	0.201	1.94
FRO99040S	3.68	1.72	44.5	0.612	0.270	2.27
FRO99040M	5.90	3.10	71.3	0.427	0.203	2.10
Forsterite	3.06	1.04	37.0	0.384	0.197	1.95
Enstatite	3.70	3.13	44.7	0.369	0.188	1.96
Allende	2.44	3.42	29.5	0.519	0.266	1.95

Therefore, the $P_{\rm max}$ tends to increase as $x_{\rm eff}$ increases (Figs 7 and 8). The majority of the grains in the forsterite sample belong to the Rayleigh and resonance ($x_{\rm eff} \approx \lambda$) domains where the dependence of $P_{\rm max}$ with size is nearly opposite, i.e. it increases as $x_{\rm eff}$ decreases (Fig. 9).

The degree of linear polarization curves for the Allende meteorite sample at three wavelengths (442, 520, and 633 nm) are plotted in Fig. 10. As shown in Fig. 1, the Allende sample mainly consists of particles in the Rayleigh and resonance regimes. In this case there is no clear trend of $P_{\rm max}$ with wavelength. The higher Fe content of the Allende meteorite compared to forsterite indicates a higher imaginary part of the refractive index at shorter wavelengths, implying a higher reflectance at red wavelengths. According to the Umov effect, the larger reflectance, the lower the maximum of the degree of linear polarization. Thus, the increase of $P_{\rm max}$ with wavelength seems to be balanced by a lower albedo at shorter wavelengths. Therefore, the maximum of the degree of linear polarization is dependent not only on the size of the grains but also on their refractive index. A study of tholins generated in plasma with different size distributions by Hadamcik et al. (2009) is in line with our results, showing that in Rayleigh regime $P_{\rm max}$ decreases when the particle size increases, while in optical regime $P_{\rm max}$ increases with the particle size.

It is worth noting that in the case of the forsterite sample (Fig. 9), the inversion angle α_0 does not change with wavelength. However, some wavelength dependence of the negative branch minimum can be distinguished at 633 nm. In the case of the Allende sample, both the minimum of the negative branch and the inversion angle vary with wavelength. The apparent dependence of the negative branch parameters on composition (i.e. refractive index) seems to be in agreement with the simulations of Zubko et al. (2009) and Zubko, Videen & Shkuratov (2015), which demonstrate that the negative polarization parameters strongly depend not only on size parameter but also on the material absorption properties.

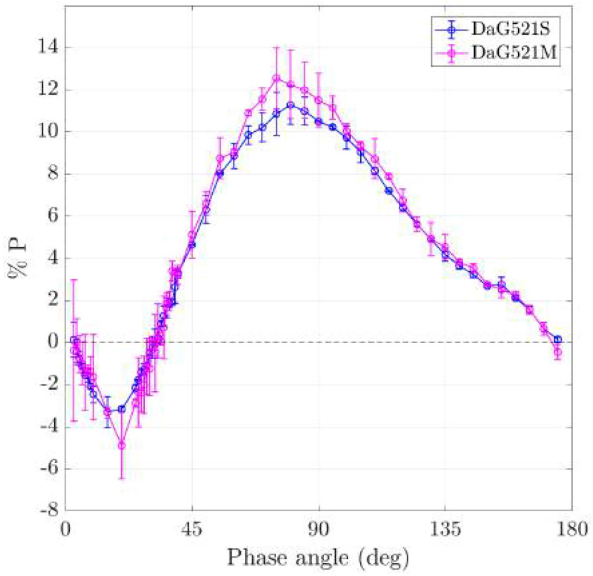

Figure 7. Measured degree of linear polarization curves for the DaG521S (blue symbols) and DaG521M (magenta symbols) samples at 520 nm.

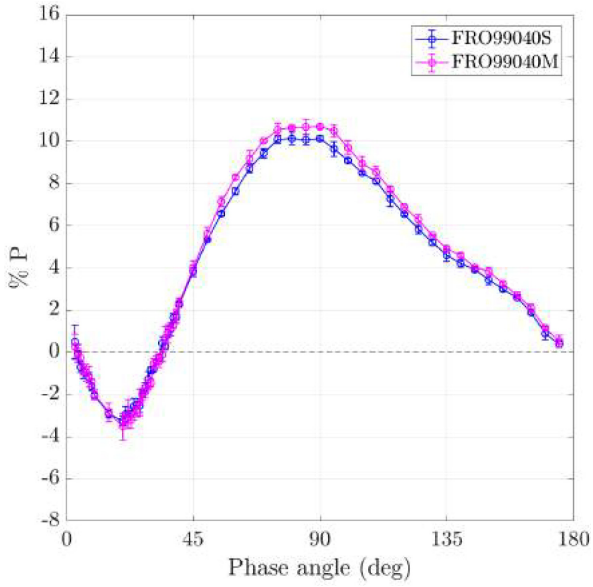

Figure 8. Measured degree of linear polarization curves for the FRO99040S (blue symbols) and FRO99040M (magenta symbols) at 520 nm.

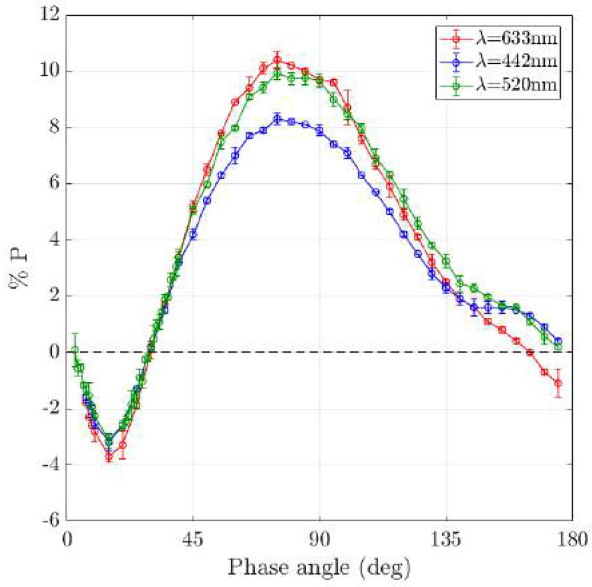

Figure 9. Measured degree of linear polarization curves for the forsterite sample at three different wavelengths.

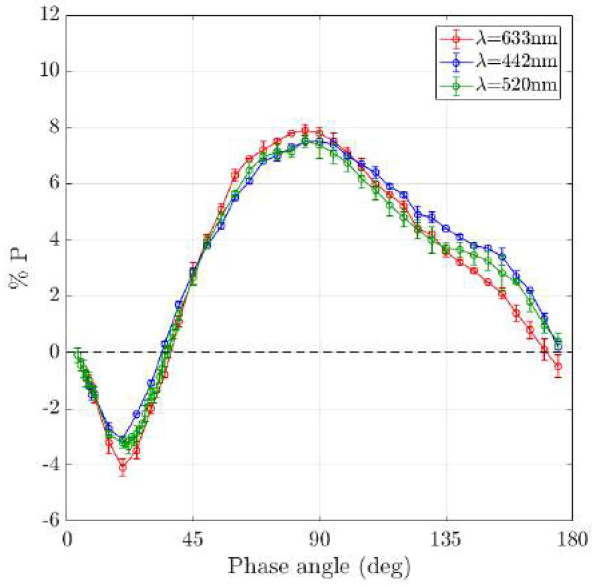

Figure 10. Measured degree of linear polarization curves for the Allende sample at three different wavelengths.

5.4 Comparison with asteroids and comets

Ground-based observations of the intensity of light scattered by cometary dust grains are usually limited to certain observational geometries. Moreover, time variations of the brightness of the coma as observed from Earth do not only depend on the phase angle but also on changes of the dust production rate as the comet moves in its orbit around the Sun (see e.g. Kolokolova et al. 2004). The OSIRIS camera onboard the Rosetta spacecraft revealed the behaviour of comet 67P phase functions from inside the coma (Bertini et al. 2017). They were obtained in a short time period (about 2.5 h) covering an unprecedented broad phase angle range (from ∼10° to ∼155°). The measured phase functions show a peculiar u-shape with a minimum at a phase angle around 100°. That phase function is not reproduced by any of the μm-sized randomly oriented particles studied in this work or previously presented in the Amsterdam–Granada Light Scattering Data base (Muñoz et al. 2012). However, laboratory measurements of the phase function of mm-sized particles (Muñoz et al. 2017) show a distinct behaviour compared to μm-sized particle clouds, with a minimum placed at much larger phase angles more in line with the 67P phase curve. Further, recent analysis of the OSIRIS phase functions at low phase angles provides a range of BSE values broader [1.7–3.6] (Bertini et al. 2018) than that based on ground-based observations [1.7–2.7] (Ishiguro et al. 2013). As shown in Table 4, the BSE values obtained for our μm-sized cometary dust analogues are within the range obtained from ground-based observations. The highest BSE value

obtained from the OSIRIS data (3.6) seem to be produced by a cloud of decimetric chunks orbiting 67P nucleus at distances smaller than 100 km (Bertini et al. 2018). All in all our experimental data suggest that 67P phase function is not dominated by randomly oriented μm-sized particles in line with the conclusions of multiinstrument analysis onboard Rosetta (Guettler, in preparation).

Polarization is a powerful tool to investigate the nature of particles populating cometary comae and asteroidal regoliths. The value of the minimum of the degree of linear polarization together with the slope of polarization curve is generally used to determine the albedo of asteroids. Moreover, polarimetric criteria are used to classify and refine the asteroid taxonomy (Belskaya et al. 2017). A caveat to direct comparisons between observations and laboratory results is that the assumption of single scattering is no longer valid for such bodies, since they are covered by a layer of regolith. Single scattering is considered to be more adequate to explain the behaviour of low-albedo objects, for which multiple scattering is less important. As a result of multiple scattering the minimum polarization value approaches zero, and the inversion angle α_0 decreases. Further, the positive polarization maximum decreases by multiple scattering effects and therefore its slope (Shkuratov et al. 2004, 2006, 2007). We refer to Kolokolova, Hough & Levasseur-Regourd (2015, chapters 5 and 8) for recent reviews on photometric and polarimetric laboratory measurements of particulate surfaces and individual particles. Taking into account the mentioned multiple scattering effects, we can still retrieve information on the physical properties that determines the observed polarimetric features of asteroidal regolith particles by direct comparison with our experimental data. For instance, in the case of (the still few) Near-Earth Asteroids (NEA) observed so far, the maximum of positive polarization can reach, for low-albedo objects like (3200) Phaethon and (101955) Bennu, much higher values of linear polarization (up to 40 per cent), well above the limits reached by the samples analysed in this work. The covered interval of angles did not include α_{max} but the observed data indicate that P_{max} could occur around 130°. Taking into account the decrease of P_{max} due to multiple scattering effects on the regolith layer, we can expect an even larger P_{max} for the single particles forming the regolith. According to previous experimental (Escobar-Cerezo et al. 2018) and computational (Liu et al. 2015) results, a high value of P_{max} shifted towards large phase angles, suggests a surface covered by particles significantly larger than those studied in this work.

Further, spectropolarimetric data of asteroids show that the gradient of linear polarization for increasing wavelength depends on the taxonomic class and upon the phase angle. In the positive polarization branch, the polarization tends to decrease for increasing wavelength for S-class objects (moderate albedo). Similar dependence of P_{max} with λ has been found for single particles that present a significantly higher imaginary part of the refractive index, k, at short (488 nm) than at large (647 nm) wavelengths (Dabrowska et al. 2015). Low-albedo objects do just the opposite as is the case of dust samples with a flat (Fig. 9) or moderate dependence of k with the wavelength (10). Note also that, for any given object of any class, the polarimetric gradient changes sign if the object is observed in the negative or in the positive polarization branch (Bagnulo, Cellino & Sterzik 2015) as is the case of the forsterite and Allende samples studied in this work (Figs 9 and 10).

On the other hand, the angle of inversion of polarization of asteroids is usually around 20°. A few objects exhibit an inversion angle at lower phase angles (15°–17°). Only a few rare objects, the so-called Barbarians, show high values of inversion angles, up to 28° (Cellino et al. 2006; Devogèle et al. 2018). As shown in Section 5.1, for the size range of the samples presented in this work, the position of the inversion angle depends on sample composition. This is also found by Devogèle et al. (2018) in their analysis of Barbarian asteroids. Other observed polarimetric evidence (P_{min} versus inversion angle plot) suggests that these objects should have a very fine surface regolith. This is also in agreement with some estimate of a low thermal inertia for (21) Lutetia, which has also a large inversion angle, not much smaller than that of Barbarians (Cellino et al. 2016). Only S-class NEAs objects have P_{max} values (7 per cent and 10 per cent) compatible with our measurements. As opposite, there are no asteroids reaching negative polarization deeper than −2,−3 per cent.

The condition of single scattering holds for cometary comae. Observational data show the existence of two classes of comets, based on the degree of linear polarization (Levasseur-Regourd et al. 1996; Shestopalov & Golubeva 2017). The high polarization comets, which are considered dust rich, and the low polarization comets, which have a higher gas component (Table 5). The measurements of the samples presented in this work seems to be of the order of the low polarization group. Generally, cometary comae behave qualitatively in a similar manner to our analogue particle clouds: they show a negative polarization branch at small phase angles, and a bell-shaped curve at side and backscattering angles, with a maximum of polarization at a phase angle near 90°. However, the exact parameters defining the cometary polarization phase curve (see Table 5 for comet 67P in particular), are different from our laboratory measurements. The 67P polarization phase curve might be shaped by particles larger than the wavelength, but with wavelength-scale surface features that could produce a polarization roughly similar that of a cloud of isolated scatterers. Moreover, the h slope observed for 67P seems to indicate that it belongs to the family of 'high polarization' comets (Rosenbush et al. 2017). This might be in agreement with the depletion of small particles (<1 μm) observed with Rosetta.

Our laboratory data support the interpretation of the decreasing polarization outward the nucleus of 67P, according to which this results from larger particles near the nucleus and smaller particles moving away from it (Rosenbush et al. 2017). In order to enable a more consistent comparison between astronomical observations and laboratory data, future studies need to consider more appropriate mixtures of components such as silicates, organics, and ices, with improved control on other characteristics such as size, shape, and surface roughness.

6 CONCLUSIONS

Our results are summarized as follows:

(i) All measured phase functions present the typical behaviour of μm-sized irregular compact dust particles in random orientation. They show strong peaks at large phase angles, almost no structure at side phase angles and soft increase at small phase angles.

(ii) The measured values of BSE of our samples are within the range obtained from ground-based observations of cometary comae. According to our experimental data small BSE values seem to indicate a coma population of μm-sized grains.

(iii) The dependence of P_{max} with size is opposite for particle sizes belonging to Rayleigh-resonance ($x_{eff} \approx \lambda$) and geometric optic ($x_{eff} \gg \lambda$) regimes. When particles are smaller or of the order of the wavelength (Rayleigh-resonance regimes), P_{max} decreases with size whereas in the geometric optics regime P_{max} tend to increase with size.

Table 5. Polarimetric parameters of two classes of comets from Levasseur-Regourd, Hadamcik & Renard (1996). Values for 67P correspond to post-perihelion period and are taken from Hadamcik et al. (2016). *The *h* value for 67P is the slope at the inversion angle, since no value for P_{max} are available.

Comet	λ (nm)	P_{min} (per cent)	α_{min} (°)	α_0 (°)	P_{max} (per cent)	α_{max} (°)	h (per cent/deg)
High P_{max}	515	-1.5 ± 0.5	9 ± 2	22.2 ± 0.5	26 ± 2	103 ± 10	0.22 ± 0.02
	670	-1.5 ± 0.5	11 ± 2	22.6 ± 0.5	28 ± 3	95 ± 10	0.25 ± 0.03
Low P_{max}	515	-1.7 ± 0.5	6 ± 3	19.0 ± 0.5	10 ± 3	80 ± 10	0.20 ± 0.02
	670	-1.9 ± 0.5	6 ± 3	20.5 ± 0.5	18 ± 3	95 ± 10	0.22 ± 0.02
67P	red	-1.7 ± 0.1	12 ± 3	22 ± 2	-	-	0.35 ± 0.02*

(iv) For the range of sizes of our samples, the minimum of the negative polarization branch seems to be dependent on both size and composition of the grains whereas the inversion angle value, α_0, depends on the refractive index.

(v) The measured degree of linear polarization curves are qualitatively similar to those obtained from ground-based observations of cometary comae. This is in line with the finding that the main scatterers in the coma are larger than the wavelength of the incident light, where the surface features of the particles are of the order of the incident wavelength.

ACKNOWLEDGEMENTS

The authors are grateful with the Museo dell'Antartide Felice Ippolito, Siena for providing the meteorite samples required, with the Department of Geoscience of the University of Padua for providing the laboratory facilities necessary to produce the samples. We are indebted to Rocío Márquez from the Scientific Instrumentation centre of the University of Granada for providing the SEM images and with Maurizio Gemelli from the Department of Earth Science of the University of Pisa. This work has been supported by the Plan Nacional de Astronomía y Astrofísica contract AYA2015-67152-R.

REFERENCES

A'Hearn M. F. et al., 2005, Science, 310, 258
A'Hearn M. F. et al., 2011, Science, 332, 1396
Bagnulo S., Cellino A., Sterzik M. F., 2015, MNRAS, 446, L11
Bardyn A. et al., 2017, MNRAS, 469, S712
Belskaya I. et al., 2017, European Planetary Science Congress, 11, EPSC2017
Bertini I. et al., 2017, MNRAS, 469, S404
Bertini I. et al., 2018, MNRAS, 482, 2924
Bertini I., Thomas N., Barbieri C., 2007, A&A, 461, 351
Blum J., Wurm G., 2008, ARA&A, 46, 21
Blum J., Gundlach B., Mühle S., Trigo-Rodriguez J. M., 2014, Icarus, 235, 156
Brassé C., 2014, , PhD thesis, Paris Est Créteil University
Brassé C., Muñoz O., Coll P., Raulin F., 2015, Planet. Space Sci., 109, 159
Brassé C., Buch A., Coll P., Raulin F., 2017, Astrobiol., 17, 8
Brearley A. J., Jones R. H., 1998, in Papike J.J., ed., Planetary materials, Chondritic meteorites. p. 3
Cellino A., Belskaya I. N., Bendjoya P., Di Martino M., Gil-Hutton R., Muinonen K., Tedesco E. F., 2006, Icarus, 180, 565
Cellino A., Bagnulo S., Tanga P., Novaković B., Delbò M., 2014, MNRAS, 439, L75
Cellino A., Bagnulo S., Gil-Hutton R., Tanga P., Canada-Assandri M., Tedesco E. F., 2016, MNRAS, 455, 2091
Chen J. H., Wasserburg G. J., 1981, Earth Planet. Sci. Lett., 52, 1
Clemett S. J., Sandford S. A., Nakamura-Messenger K., Hörz F., McKay D. S., 2010, Meteorit. Planet. Sci., 45, 701
Combe J.-P. et al., 2017, in Lunar and Planetary Science Conference. p. 2849
Crovisier J., Leech K., Bockelee-Morvan D., Brooke T. Y., Hanner M. S., Altieri B., Keller H. U., Lellouch E., 1997, Science, 275, 1904
Dabrowska D. D., Muñoz O., Moreno F., Ramos J. L., Martínez-Frías J., Wurm G., 2015, Icarus, 250, 83
DeMeo F., Binzel R. P., 2008, Icarus, 194, 436
Devogèle M. et al., 2018, Icarus, 304, 31
Dorschner J., Begemann B., Henning T., Jaeger C., Mutschke H., 1995, A&A, 300, 503
Escobar-Cerezo J. et al., 2018, ApJS, 235, 19
Escobar-Cerezo J., Palmer C., Muñoz O., Moreno F., Penttilä A., Muinonen K., 2017, ApJ, 838, 74
Frattin E. et al., 2017, MNRAS, 469, S195
Fray N. et al., 2017, MNRAS, 469, S506
Fulle M. et al., 2016, MNRAS, 462, S132
Fulle M., Blum J., 2017, MNRAS, 469, S39
Gladstone e. a., 2016, Science, 351, aad8866
Grossman J. N., 1999, Meteorit. Planet. Sci., 34, 169
Hadamcik E., Renard J.-B., Alcouffe G., Cernogora G., Levasseur-Regourd A. C., Szopa C., 2009, Planet. Space Sci., 57, 1631
Hadamcik E., Levasseur-Regourd A. C., Hines D. C., Sen A. K., Lasue J., Renard J.-B., 2016, MNRAS, 462, S507
Hanner M. S., Bradley J. P., 2004, Comets II, Composition and mineralogy of cometary dust, University of Arizona Press, Tucson, Arizona, p. 555
Hansen J. E., Travis L. D., 1974, Space Sci. Rev., 16, 527
Hasenkopf C. A., Beaver M. R., Trainer M. G., Langley Dewitt H., Freedman M. A., Toon O. B., McKay C. P., Tolbert M. A., 2010, Icarus, 207, 903
Hörz F. et al., 2006, Science, 314, 1716
Hovenier J. W., Guirado D., 2014, J. Quant. Spectrosc. Radiat. Transfer, 133, 596
Ishiguro M., Yang H., Usui F., Pyo J., Ueno M., Ootsubo T., Minn Kwon S., Mukai T., 2013, ApJ, 767, 75
Johansen A., Youdin A., 2007, ApJ, 662, 627
Jost B., Pommerol A., Poch O., Brouet Y., Fornasier S., Carrasco N., Szopa C., Thomas N., 2017, Planet. Space Sci., 148, 1
Kissel J., Krueger F. R., 1987, Nature, 326, 755
Kolokolova L., Hanner M. S., Levasseur-Regourd A.-C., Gustafson B. Å. S., 2004, Comets II, Physical properties of cometary dust from light scattering and thermal emission, University of Arizona Press, Tucson, Arizona, p. 577
Kolokolova L., Hough J., Levasseur-Regourd A.-C., 2015, Polarimetry of Stars and Planetary Systems, Cambrige University Press, Cambrige
Krot A. N., Scott E. R. D., Zolensky M. E., 1995, Meteoritics, 30, 748
Krot A. N., Petaev M. I., Scott E. R. D., Choi B.-G., Zolensky M. E., Keil K., 1998, Meteorit. Planet. Sci., 33, 1065
Levasseur-Regourd A. C., Hadamcik E., Renard J. B., 1996, A&A, 313, 327
Lisse C. M., Kraemer K. E., Nuth J. A., Li A., Joswiak D., 2007, Icarus, 187, 69
Liu L., Mishchenko M. I., Hovenier J. W., Volten H., Muñoz O., 2003, J. Quant. Spectrosc. Radiat. Transfer, 79, 911
Liu J., Yang P., Muinonen K., 2015, J. Quant. Spectrosc. Radiat. Transfer, 161, 136
Maas R. W., Ney E. P., Woolf N. J., 1970, ApJ, 160, L101
Mackowski D. W., Mishchenko M. I., 1996, J. Opt. Soc. Am. A, 13, 2266
Mahnes G., Göpel C., Allégre C. J., 1987, Meteoritics, 22, 453

Matrajt G. et al., 2008, Meteorit. Planet. Sci., 43, 315
McSween H. Y., Jr., 1977, Geochim. Cosmochim. Acta, 41, 477
Muinonen K., Mishchenko M. I., Dlugach J. M., Zubko E., Penttilä A., Videen G., 2012, ApJ, 760, 118
Muñoz O. et al., 2010, J. Quant. Spectrosc. Radiat. Transfer, 111, 187
Muñoz O., Volten H., de Haan J. F., Vassen W., Hovenier J. W., 2000, A&A, 360, 777
Muñoz O., Moreno F., Guirado D., Ramos J. L., Volten H., Hovenier J. W., 2011, Icarus, 211, 894
Muñoz O., Moreno F., Guirado D., Dabrowska D. D., Volten H., Hovenier J. W., 2012, J. Quant. Spectrosc. Radiat. Transfer, 113, 565
Muñoz O., Moreno F., Vargas-Martín F., Guirado D., Escobar-Cerezo J., Min M., Hovenier J. W., 2017, ApJ, 846, 85
Nittler L. R., McCoy T. J., Clark P. E., Murphy M. E., Trombka J. I., Jarosewich E., 2004, Antarct. Meteorit. Res., 17, 231
Poch O., Pommerol A., Jost B., Carrasco N., Szopa C., Thomas N., 2016a, Icarus, 266, 288
Poch O., Pommerol A., Jost B., Carrasco N., Szopa C., Thomas N., 2016b, Icarus, 267, 154
Rawle A. F., 1993, The Basic Principles of Particle Size Analysis, Malvern Instruments, UK
Reinhard R., 1986, Nature, 321, 313
Rosenbush V. K., Ivanova O. V., Kiselev N. N., Kolokolova L. O., Afanasiev V. L., 2017, MNRAS, 469, S475
Sagan C., Khare B. N., 1979, Nature, 277, 102
Sagdeev R. Z. et al., 1986, Nature, 321, 262
Sandford S. A. et al., 2006, Science, 314, 1720
Schulze H., Kissel J., Jessberger E. K., 1997, in Pendleton Y. J., ed., ASP Conf. Ser. , Vol. 122, From Stardust to Planetesimals. Astron. Soc. Pac., San Francisco, p. 397
Shestopalov D. I., Golubeva L. F., 2017, Adv. Space Res., 59, 2658
Shkuratov Y., Ovcharenko A., Zubko E., Volten H., Munoz O., Videen G., 2004, J. Quant. Spectrosc. Radiat. Transfer, 88, 267
Shkuratov Y., Bondarenko S., Ovcharenko A., Pieters C., Hiroi T., Volten H., Muñoz O., Videen G., 2006, J. Quant. Spectrosc. Radiat. Transfer, 100, 340
Shkuratov Y., Bondarenko S., Kaydash V., Videen G., Muñoz O., Volten H., 2007, J. Quant. Spectrosc. Radiat. Transfer, 106, 487
Sierks H. et al., 2015, Science, 347, aaa1044
Soderblom L. A. et al., 2002, Science, 296, 1087
van de Hulst H. C., 1957, Light Scattering by Small Particles, John Wiley and Sons , New York
Volten H., Muñoz O., Brucato J. R., Hovenier J. W., Colangeli L., Waters L. B. F. M., van der Zande W. J., 2006, J. Quant. Spectrosc. Radiat. Transfer, 100, 429
Weisberg M. K., McCoy T. J., Krot A. N., 2006, Systematics and Evaluation of Meteorite Classification. Univ. of Arizona, Tucson, p. 19
Zolensky M. E. et al., 2006, Science, 314, 1735
Zubko E., 2015, Opt. Lett., 40, 1204
Zubko E., Kimura H., Shkuratov Y., Muinonen K., Yamamoto T., Okamoto H., Videen G., 2009, J. Quant. Spectrosc. Radiat. Transfer, 110, 1741
Zubko E., Videen G., Shkuratov Y., Muinonen K., Yamamoto T., 2011, Icarus, 212, 403
Zubko E., Videen G., Shkuratov Y., 2015, J. Quant. Spectrosc. Radiat. Transfer, 151, 38
Zubko E., Videen G., Zubko N., Shkuratov Y., 2017, J. Quant. Spectrosc. Radiat. Transfer, 190, 1
Zubko E., Videen G., Zubko N., Shkuratov Y., 2018, MNRAS, 477, 4866

This paper has been typeset from a TEX/LATEX file prepared by the author.